Trends in Computational and Applied Mathematics, **26** (2025), e01843
Sociedade Brasileira de Matemática Aplicada e Computacional
Online version ISSN 2676-0029 www.scielo.br/tcam
ORIGINAL ARTICLE
doi: 10.5540/tcam.2025.026.e01843

Numerical simulations of two-phase electroosmotic shearing with viscoelastic fluids

DANIEL G. L. RAYMUNDO[1], ALEXANDRE MIGUEL P. AFONSO[2] and ANTONIO CASTELO FILHO[3]

Received on November 25, 2024 / Accepted on November 3, 2025

ABSTRACT. This article investigates the numerical modeling and two-dimensional simulation of electroosmotic two-phase flows involving complex fluids in rectangular channels with no pressure difference. We apply mainly the nonlinear Poisson-Boltzmann (PB) model for charge distribution coupled to the Navier-Stokes equations, constitutive equations for viscoelastic fluids, and the interface transport by Volume-of-Fluid with Piecewise-Linear Interface Construction. The numerical framework is implemented in the *HiG-Flow* system, which simulates incompressible flows in hierarchical cartesian meshes of arbitrary refinement represented by generalized trees with interpolations by a robust meshless moving least squares method. In two-phase systems, we analyze droplet deformation under both neutral and electroosmotic shear, exploring the impact of permittivity variations between matrix and droplet fluids. Our results suggest that the Korteweg-Helmholtz force may play a crucial role in interface deformation patterns, while viscoelasticity demonstrates itself capable of moderating surface tension effects and stabilizing deformations in uniform and non-uniform permittivity cases.

Keywords: numerical eletroosmosis, two-phase flows, viscoelastic drop shearing.

1 INTRODUCTION

The growing demand for miniaturized devices in biotechnology and chemical engineering has sparked significant interest in electrokinetic phenomena, particularly electroosmotic flows (EOFs). An important application is Lab-on-a-chip systems, which enable laboratory experiments to be performed on micro- or nanometric-scale chips, reducing costs and sample volumes to nanoliters or even picoliters while offering faster production cycles and improved safety [54].

*Corresponding author: Alexandre Miguel Prior Afonso – E-mail: aafonso@fe.up.pt
[1]ICMC-USP, São Paulo, Brazil – E-mail: hobitteras@usp.br https://orcid.org/0000-0003-1610-5504
[2]Faculdade de Engenharia da Universidade do Porto, Departamento de Engenharia Mecânica, Centro de Estudos de Fenómenos de Transporte (CEFT), Porto, Portugal – E-mail: aafonso@fe.up.pt https://orcid.org/0000-0003-2825-0709
[3]Universidade de São Paulo, Departamento de Matemática Aplicada e Estatística, ICMC, São Paulo, Brazil – E-mail: castelo@icmc.usp.br https://orcid.org/0000-0001-8009-4577

Precise control is essential in these devices, from managing electrokinetic phenomena and specialized wall coatings [37] to handling the complex behavior of viscoelastic fluids and their associated relaxation times [52]. The frequently occurring EOFs arise when an external electric field acts on mobile charges near solid surfaces, providing an elegant alternative to pressure-driven flows in microscale devices [52]. The electric double layer (EDL), consisting of the Stern layer and a diffuse layer near the walls, plays a fundamental role in this process. When subjected to an external electric field, the movement of charges in the EDL induces fluid motion that propagates to the electroneutral center region through viscous effects.

Comparably significant for microfluidic flows is the interaction between two or more immiscible fluids, which presents both challenges and opportunities for chemical separation and mixing processes [18,22]. The canonical problem of an isolated droplet under shear flow serves as a fundamental model for understanding these interactions [16], with deformation and breakup patterns directly influenced by fluid viscoelasticity [25], while the concentration of nonpolar solvents affects electrophoretic and electroosmotic mobility [13]. The combination of these effects with electrokinetic phenomena creates a rich and complex system worthy of detailed investigation and recent advances in computational capability have enabled increasingly sophisticated simulations of such systems. Previous work has established the foundations of electroosmotic flow modeling, from the early numerical studies of microchannel EOFs [42] to more recent investigations incorporating two-fluid systems and viscoelastic effects [2]. However, the combined effects of viscoelasticity and variable permittivity in electroosmotic shearing flows remain scarcely studied, especially from a numerical perspective.

In this work, we describe a cohesive mathematical and numerical framework for simulating purely electroosmotic two-phase flows with complex fluids, and present results of numerical simulations of singlephase transient EOFs and two-phase electroosmotic drop shearing of varying electrical permittivity with viscoelastic fluids in two-dimensional rectangular microchannels with no pressure difference. Our approach combines classical viscoelastic models, nonlinear electrokinetics and surface tension, implemented within a hierarchical cartesian mesh framework of arbitrary refinement that interpolates variables using a meshless moving least squares method [50].

Previous research has analysed each of the aforementioned flow regimes individually. Within a similar numerical framework, the doctoral thesis of Bezerra [10] investigated electroosmotic viscoelastic flows, while the master's thesis [48] and doctoral qualifying exam report [49] of Silva focused on two-phase viscoelastic flows. Notably, Figueiredo has also conducted earlier investigations on the latter type of flow [20, 21], and electroosmotic flows on non-newtonian fluids have been previously explored experimentally [33], analitically [1,17,40], and numerically [5,41,53].

2 MATHEMATICAL FRAMEWORK

2.1 Governing Equations

The foundation of our models rests on the incompressible isothermal Navier-Stokes equations [8, 43], which govern the fluid velocity and pressure fields, $\boldsymbol{u}$ and p,

$$\nabla \cdot \boldsymbol{u} = 0,$$
$$\rho \left(\frac{\partial \boldsymbol{u}}{\partial t} + \boldsymbol{u} \cdot \nabla \boldsymbol{u} \right) = -\nabla p + \nabla \cdot (\boldsymbol{\tau}_p + 2\mu_s \boldsymbol{D}) + \boldsymbol{F}_e + \boldsymbol{F}_\sigma,$$

where ρ represents the mass density, $\boldsymbol{\tau}_p$ and $\boldsymbol{D} = \frac{1}{2}\left(\nabla \boldsymbol{u} + \nabla \boldsymbol{u}^T\right)$ are the polymeric and deformation tensors, μ_s is the solvent viscosity, $\boldsymbol{F}_e$ is the electrokinetic forcing term and $\boldsymbol{F}_\sigma$ is the force per unit volume accounting for the surface tension between fluids. The incompressibility constraint is a direct consequence of the microscale assumed of the flow [8, 32].

To govern the evolution of the viscoelastic polymeric tensor $\boldsymbol{\tau}_p$, we consider the conformation (or configuration) tensor $\boldsymbol{A}$, the eigenspace of which represents the average orientations and stretching degree of local polymer chains, given by

$$\boldsymbol{A} = \frac{\lambda(1-\xi)}{\mu_p} \boldsymbol{\tau}_p + \boldsymbol{I},$$

with λ being the relaxation time of the fluid, ξ, a slip parameter, measuring non-affine motion between polymer molecules and the continuum [24], μ_p, the viscosity of the polymer, and $\boldsymbol{I}$, the identity tensor. Its constitutive equation for a variety of models, assuming the convention $(\nabla \boldsymbol{u})_{ij} = \frac{\partial u_j}{\partial x_i}$, is

$$\frac{\partial \boldsymbol{A}}{\partial t} + \boldsymbol{u} \cdot \nabla \boldsymbol{A} = \boldsymbol{A} \nabla \boldsymbol{u} + (\nabla \boldsymbol{u})^T \boldsymbol{A} - \xi \left(\boldsymbol{A}\boldsymbol{D} + \boldsymbol{D}\boldsymbol{A} \right) + \frac{1}{De} \mathscr{M}(\boldsymbol{A}), \tag{2.1}$$

with $\mathscr{M}$ being a model-dependent tensor function and $De = \frac{\lambda u_{\text{ref}}}{L}$, the Deborah number for the reference velocity u_{ref} and chacteristic length L. It can be shown that, given mild conditions, the positive-definiteness of $\boldsymbol{A}$ persists during time evolution [30]. However, constitutive equations in general present strong numerical instabilities for high Deborah numbers, the so-called high Weissenberg number problem (HWNP) [19], which can lead to a violation of positivity for computations. To alleviate those difficulties, plausibly caused by inadequate approximations of steep gradients, Fattal and Kupferman studied the logarithmic transformation of the tensor by decomposing $\nabla \boldsymbol{u}$ and rewriting (2.1) [19], a formulation that was later generalized for matrix functions $\mathbb{K}(\boldsymbol{A})$ in [3] and culminated on

$$\frac{\partial \mathbb{K}(\boldsymbol{A})}{\partial t} + \boldsymbol{u} \cdot \nabla \mathbb{K}(\boldsymbol{A}) = \boldsymbol{\Omega}\mathbb{K}(\boldsymbol{A}) - \mathbb{K}(\boldsymbol{A})\boldsymbol{\Omega} + 2\boldsymbol{O}\tilde{\boldsymbol{B}}\boldsymbol{\Lambda}\boldsymbol{J}\boldsymbol{O}^T + \frac{1}{De}\boldsymbol{O}\mathscr{M}(\boldsymbol{\Lambda})\boldsymbol{J}\boldsymbol{O}^T.$$

In this system, known as the kernel-conformation, $\boldsymbol{A} = \boldsymbol{O}\boldsymbol{\Lambda}\boldsymbol{O}^T$ is eigendecomposed,

$$\nabla \boldsymbol{u}^T - \xi \boldsymbol{D} = \boldsymbol{\Omega} + \boldsymbol{B} + \boldsymbol{N}\boldsymbol{A}^{-1},$$

with Ω and $\boldsymbol{N}$ skew-symmetric and $\boldsymbol{B}$, symmetric and comuting with $\boldsymbol{A}$, and $J_{ii} = \left(\frac{\partial \boldsymbol{K}(\boldsymbol{\Lambda})}{\partial \Lambda_{ii}}\right)_{ii}$ is diagonal. By restricting to both the Oldroyd-B [38] and the simplified Phan-Thien-Tanner (SPTT) [55] models in singlephase flow, $\xi = 0$ and

$$\mathscr{M}(\boldsymbol{\Lambda}) = \begin{cases} \boldsymbol{I} - \boldsymbol{\Lambda}, & \text{Oldroyd-B,} \\ [1 + \varepsilon \operatorname{tr}(\boldsymbol{\Lambda} - \boldsymbol{I})]\,(\boldsymbol{I} - \boldsymbol{\Lambda}), & \text{SPTT,} \end{cases}$$

with ε being defined as the mobility parameter, measuring the rate of construction of Yamamoto networks in the PTT models [34, 56].

The electrokinetic aspects are modeled through either the Poisson-Nernst-Planck (PNP) system or the Poisson-Boltzmann (PB) approximation. For symmetric ionic species concentrations c_+ and c_- of equal diffusivity D and valence Z respecting the Nernst-Einstein relation for electrophoretic mobility,

$$\mu_{EP,\pm} = \frac{\pm eDZ}{k_B T},$$

the Nernst-Planck equation takes the form

$$\frac{\partial c_\pm}{\partial t} + \nabla \cdot \left[\left(\boldsymbol{u} \pm \frac{eDZ}{k_B T} \boldsymbol{E} \right) c_\pm \right] = D \nabla^2 c_\pm,$$

where the electric field $\boldsymbol{E}$ has a potential Φ in simply-connected regions, such that $\boldsymbol{E} = -\nabla\Phi$. We have denoted the electron charge by e, the Boltzmann constant by k_B and the flow temperature by T. Together with Gauss's law and a decomposition $\Phi = \phi + \psi$, where ϕ is the applied potential and ψ is the induced potential from the EDL formation, the PNP system is

$$\begin{aligned} &\nabla \cdot (\varepsilon_e \nabla \phi) = 0, \\ &\nabla \cdot (\varepsilon_e \nabla \psi) = -\rho_e = -eZ(c_+ - c_-), \\ &\frac{\partial c_\pm}{\partial t} + \nabla \cdot \left[\left(\boldsymbol{u} \mp \frac{eDZ}{k_B T} \nabla(\phi + \psi) \right) c_\pm \right] = D \nabla^2 c_\pm, \end{aligned}$$

where ρ_e is the charge density and ε_e is the electric permittivity. When considering insulating walls, the homogenous Neumann condition $\frac{\partial \phi}{\partial \boldsymbol{n}} = 0$ applies and we assume $\psi = \zeta_0$ to be the zeta potential value on the Stern layer, very close to the wall. Under steady-state conditions with negligible convective transport and charge variations essentially normal to variations of ϕ, the PB approximation provides

$$\nabla \cdot (\varepsilon_e \nabla \psi) = 2eZc_\infty \sinh\left(\frac{eZ}{k_B T} \psi \right),$$

where we take c_∞ to be the charge in the electroneutral region. Whenever $\frac{eZ\zeta_0}{k_B T} \ll 1$, this can be linearized following Debye-Hückel theory

$$\nabla \cdot (\varepsilon_e \nabla \psi) \approx \frac{1}{\lambda_D^2} \psi,$$

with $\lambda_D = \sqrt{\frac{\varepsilon_e k_B T}{2(eZ)^2 c_\infty}}$ accounting for a characteristic thickness of the EDL, also known as the Debye length, and even though we do not solve the Poisson-Boltzmann-Debye-Hückel equation directly, transient comparisons with small ζ_0 for the PNP are simulated. It follows that a suitable Dirichlet wall condition for the charge concentrations is

$$c_\pm = c_\infty \exp\left(-\frac{eZ}{k_B T}\zeta_0\right).$$

Check [31] for a more thorough discussion on boundary conditions. Assuming the fluids to form a linear dielectric with instantaneous polarization response, the electric force is given by

$$\boldsymbol{F}_e = (\nabla \cdot \boldsymbol{D}_e)\boldsymbol{E} - \frac{1}{2}\|\boldsymbol{E}\|^2 \nabla \varepsilon_e = -\rho_e \nabla(\phi + \psi) - \frac{1}{2}\|\nabla(\phi + \psi)\|^2 \nabla \varepsilon_e,$$

called the Korteweg-Helmholtz force (KHF) [14]. Following [31], the term involving $\nabla\psi$ is omitted, formally incorporated in the pressure gradient, to avoid force imbalances that can hinder numerical convergence.

The interface between immiscible fluids forms a surface that tends to keep its minimum energy configuration by minimizing the mean curvature κ_σ, generating a force per unit area acting on the surface in the direction of its normal $\boldsymbol{n}_\sigma$ called surface tension. The continuum surface force (CSF) approach presented in [12] consists of converting this force into a body force per unit volume $\boldsymbol{F}_\sigma$ in a computational setting. Brackbill et al. use a suitable variation f of the characteristic of a reference fluid to provide an approximation to the Dirac-delta of the surface δ_σ by ∇f and the normal by $\frac{\nabla f}{\|\nabla f\|}$, developing

$$\boldsymbol{F}_\sigma = c_\sigma \kappa_\sigma \nabla f,$$

where c_σ is the surface tension coefficient, a property of interfaces measuring the proportionality between surface tension and the mean curvature vector $\kappa_\sigma \boldsymbol{n}_\sigma$. It turns out such a variation f is compatible with the volume fraction in the Volume-of-Fluid formulation of [29] for modeling free surface flows, described by

- $f = 1$ if the computational cell is in the interior of fluid 1;
- $f = 0$ if the computational cell is in the interior of fluid 0;
- $0 < f < 1$ if the computational cell contains the interface between fluids,

and which is subject to the transport equation

$$\frac{\partial f}{\partial t} + \boldsymbol{u} \cdot \nabla f = 0. \tag{2.2}$$

We can then use f to linearly interpolate the properties χ such as the dynamic viscosity of the fluid solutions, μ, the properties ρ, μ_s, μ_p, λ, ε_e, and the tensor function $\mathscr{M}$ by calculating

$$(1-f)\chi_0 + f\chi_1,$$

denoting by χ_i the property of fluid i.

2.2 Adimensionalization

Letting ρ_{ref} be a reference fluid density, μ_{ref}, a reference viscosity, and $\varepsilon_{e_{\text{ref}}}$ a reference electric permittivity, we define the adimensional variables to be

$$x_i^* = \frac{x_i}{L},\ \rho^* = \frac{\rho}{\rho_{\text{ref}}},\ \mu^* = \frac{\mu}{\mu_{\text{ref}}},\ \boldsymbol{u}^* = \frac{\boldsymbol{u}}{u_{\text{ref}}},\ De_i = \frac{\lambda_i u_{\text{ref}}}{L},$$
$$\beta_i = \frac{\mu_{s_i}}{\mu_i},\ \phi^* = \frac{\phi}{\zeta_0},\ \psi^* = \frac{\psi}{\zeta_0},\ c_\pm^* = \frac{c_\pm}{c_\infty},\ E_x^* = \frac{u_{\text{ref}} L \mu_{\text{ref}}}{\varepsilon_{e_{\text{ref}}}\zeta_0^2},$$
$$\varepsilon_e^* = \frac{\varepsilon_e}{\varepsilon_{e_{\text{ref}}}},\ \alpha = \frac{eZ\zeta_0}{k_B T},\ \delta = \frac{c_\infty e Z L^2}{\zeta_0 \varepsilon_{e_{\text{ref}}}},\ Pe = \frac{u_{\text{ref}} L}{D},\ \kappa = \frac{L}{\lambda_D},$$

where Pe is the Péclet number and E_x is the electric field magnitude obtained by equating the reference velocity u_{ref} with the Helmholtz-Smoluchowski velocity $u_{HS} = \frac{\varepsilon_{e_{\text{ref}}}\zeta_0}{\mu_{\text{ref}}} E_x$. *Dropping* the * superscripts and assuming properties to be constant in *each* fluid, it follows that the interpolations with the volume fraction f are

$$\rho = (1-f)\rho_0 + f\rho_1, \quad \mu = (1-f)\mu_0 + f\mu_1, \quad De = (1-f)De_0 + fDe_1,$$
$$\beta = \frac{(1-f)\beta_0\mu_0 + f\beta_1\mu_1}{(1-f)\mu_0 + f\mu_1}, \quad \mathscr{M} = (1-f)\mathscr{M}_0 + f\mathscr{M}_1, \quad \varepsilon_e = (1-f)\varepsilon_{e_0} + f\varepsilon_{e_1},$$

defining the tensor functions $\mathscr{M}_i$ as

$$\mathscr{M}_i(\boldsymbol{\Lambda}) = \begin{cases} \boldsymbol{I} - \boldsymbol{\Lambda}, & \text{Oldroyd-B}, \\ [1 + \varepsilon_i \operatorname{tr}(\boldsymbol{\Lambda} - \boldsymbol{I})](\boldsymbol{I} - \boldsymbol{\Lambda}), & \text{SPTT}, \end{cases}$$

for the resolution of different models in the same flow. If one of the fluids is newtonian, $\mathscr{M}_i$ and De are set to 0 and $\beta = 1$, while for cells fully embedded in newtonian fluid, $\boldsymbol{A} = \boldsymbol{I}$. Together, the adimensionalized systems are written

$$\nabla \cdot \boldsymbol{u} = 0,$$
$$\rho\left(\frac{\partial \boldsymbol{u}}{\partial t} + \boldsymbol{u}\cdot\nabla\boldsymbol{u}\right) = -\nabla p + \nabla\cdot\left(\boldsymbol{\tau}_p + \frac{2\beta\mu}{Re}\boldsymbol{D}\right) + \frac{1}{ReE_x}\boldsymbol{F}_e + \boldsymbol{F}_\sigma,$$
$$\frac{\partial \mathbb{K}(\boldsymbol{A})}{\partial t} + \boldsymbol{u}\cdot\nabla\mathbb{K}(\boldsymbol{A}) = \boldsymbol{\Omega}\mathbb{K}(\boldsymbol{A}) - \mathbb{K}(\boldsymbol{A})\boldsymbol{\Omega} + 2\boldsymbol{O}\tilde{\boldsymbol{B}}\boldsymbol{\Lambda}\boldsymbol{J}\boldsymbol{O}^T + \frac{1}{De}\boldsymbol{O}\mathscr{M}(\boldsymbol{\Lambda})\boldsymbol{J}\boldsymbol{O}^T,$$
$$\nabla\cdot(\varepsilon_e\nabla\phi) = 0,$$
$$\nabla\cdot(\varepsilon_e\nabla\psi) = -\rho_e = \begin{cases} -\delta(c_+ - c_-), & \text{PNP}, \\ 2\delta\sinh(\alpha\psi) \approx \kappa^2\psi, & \text{PB}, \end{cases}$$
$$\frac{\partial c_\pm}{\partial t} + \nabla\cdot\left[\left(\boldsymbol{u} \mp \frac{\alpha}{Pe}\nabla(\phi+\psi)\right)c_\pm\right] = \frac{1}{Pe}\nabla^2 c_\pm,$$
$$\frac{\partial f}{\partial t} + \boldsymbol{u}\cdot\nabla f = 0,$$

coupled to

$$\boldsymbol{\tau}_p = \frac{(1-\beta)\mu}{ReDe(1-\xi)}(\boldsymbol{A}-\boldsymbol{I}),$$
$$\boldsymbol{F}_e = -\rho_e \nabla\phi - \frac{1}{2}\|\nabla(\phi+\psi)\|^2 \nabla\varepsilon_e,$$
$$\boldsymbol{F}_\sigma = \frac{1}{ReCa}\kappa_\sigma \nabla f,$$

in which $Ca = \frac{u_{\text{ref}}\mu_{\text{ref}}}{\sigma}$ is the capillary number.

3 *HiG-Flow*

HiG-Flow is a finite difference staggered grid numerical simulation C library designed to solve a variety of incompressible flow regimes, including two-phase [48], viscoelastic and electroosmotic [11] in arbitrarily refined cartesian meshes [50]. It was created over the *HiG-Tree* system, a parallel hierarchical mesh partial differential equation (PDE) solver using the Message Passing Interface (MPI) framework for process comunication, the boost/geometry package for determining process overlap, and the Zoltan library for domain decomposition. The *HiG-Tree* divides mesh domains in hyper-rectangular regions composed of generalized trees, such as quad- and octrees (see Figure 1), and evaluates properties θ in arbitrary points $\boldsymbol{p}$ by polynomial approximations Θ using nearby sampled points $\boldsymbol{p}_i$, implementing a meshless robust least squares method that minimizes the weighted error

$$\mathscr{E}(\boldsymbol{c}) = \sum_{i=1}^{m} \frac{1}{\|\boldsymbol{p}-\boldsymbol{p}_i\|^2}\left(\Theta(\boldsymbol{p}_i) - \theta(\boldsymbol{p}_i)\right)^2$$

by a QR decomposition – that is, closer points are given more importance in the interpolation. Accurate evaluations are crucial for discretization stencils in coarse-to-fine grid transitions.

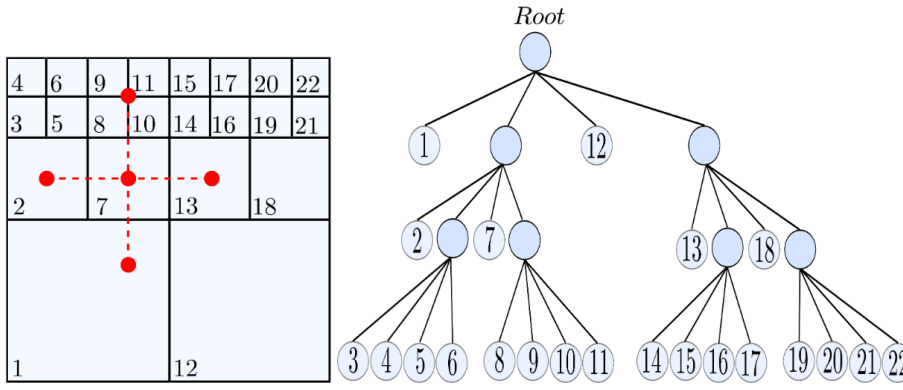

Figure 1: Example of a stencil on a hierarchical grid (left) represented by a quadtree (right) – from [9].

The *HiG-Flow* solves the sparse linear systems arising from the PDE discretizations by filling global matrix rows and calling the KSP interface of the Portable, Extensible Toolkit for Scientific Computation (PETSc) [7]. Boundaries are solved implicitly, evaluating properties outside the domain and adding the interpolated values to the right-hand side of the linear systems. The KSP interface applies iterative preconditioned Krylov Subspace (KS) methods to the assembled linear problems, from which we choose the flexible BiCGStab (Biconjugate gradient stabilized) method [15] with the algebraic multigrid preconditioner BoomerAMG from HYPRE, offering customized parallel multigrid smoothing [28]. The stopping criterion at the kth (inner) iteration of the KS methods are implemented as

$$\|\mathrm{res}^k\| < \max\left(\mathrm{tol}_r\|\mathrm{res}^0\|,\mathrm{tol}_{\mathrm{abs}}\right),$$

where the norm type is chosen by the user (2-norm by default), res^k is the computed residual at the kth iteration, tol_r is the relative tolerance, $\mathrm{tol}_{\mathrm{abs}}$, the absolute tolerance, and we set $\mathrm{tol}_{\mathrm{abs}} = 10^{-10}$ and $\mathrm{tol}_r = 10^{-14}$. Regarding timestepping iterations n, the singlephase simulations, which aim to halt at steady state, are set to stop whenever

$$\left|\|\boldsymbol{u}^n - \boldsymbol{u}^{(n-1)}\|_2\right| < \max\left(10^{-10}, 10^{-5}\Delta t\right),$$

with Δt the time increment.

4 NUMERICAL METHODS

To avoid pressure-velocity decoupling in finite difference methods, the *HiG-Flow* adopts a staggered (or marker-and-cell) grid arrangement, where the velocities and forces are located in cell faces and the remaining properties are stored in cell centers, including tensor components, while every boundary value is face centered [27]. Since the momentum relations should be used to update the velocity field due to the time derivative, an equation is required to numerically solve for pressure, while keeping the incompressibility constraint. To that end, a fractional step method of the incremental projection type is employed [51]. Letting the superscript n refer to the n-th timestep of a time-discretized variable, $\mathscr{C}$ to the nonlinear space-discretized convective term, $\mathscr{T}$ to the stress-tensor term, and $\mathscr{F}$ to the forcing terms, the procedure to solve the Navier-Stokes is written

$$\tilde{\boldsymbol{u}}^{n+1} = \boldsymbol{u}^n + \Delta t\left[-\mathscr{C}\left(\tilde{\boldsymbol{u}}^{n+1/2}, \boldsymbol{u}^n\right) + \frac{1}{\rho^{n+1/2}}\left(-\nabla p^{n-1/2} + \mathscr{T}^n\left(\tilde{\boldsymbol{u}}^{n+1}, \tilde{\boldsymbol{u}}^{n+1/2}, \boldsymbol{u}^n\right) + \mathscr{F}^{n+1/2}\right)\right],$$

$$\nabla\cdot\left(\frac{1}{\rho^{n+1/2}}\nabla\left(\Delta p^n\right)\right) = \frac{1}{\Delta t}\nabla\cdot\tilde{\boldsymbol{u}}^{n+1},$$

$$\boldsymbol{u}^{n+1} = \tilde{\boldsymbol{u}}^{n+1} - \Delta t\frac{1}{\rho^{n+1/2}}\nabla\left(\Delta p^n\right),$$

$$p^{n+1/2} = p^{n-1/2} + \Delta p^n,$$

with $\Delta p^n = \left(p^{n+1/2} - p^{n-1/2}\right)$. For closure, an initial condition for pressure is necessary, homogenous Neumann boundary conditions are imposed on Δp wherever a $\boldsymbol{u}$ Dirichlet boundary is

present and the boundary values of $\tilde{\boldsymbol{u}}$ and $\boldsymbol{u}$ are required to be the same. The dependence of $\mathscr{T}$ on the time $n+1$ represents the usage of semi-implicit methods due to severe Courant conditions of diffusion relative to convection, for which $\nabla\cdot\left(\frac{\beta\mu}{Re}\nabla\boldsymbol{u}\right)$ is solved implicitly to allow for a feasible time resolution. The incremental projection also has a second order coupling error in $\boldsymbol{u}$, helping overcome excessive time restrictions [51].

Time integration is performed using Explicit Euler on the constitutive equations, backwards Euler on the Nernst-Planck equations, and a trapezoidal backwards differentiation formula of second order on the momentum equations of the intermediate velocity $\tilde{\boldsymbol{u}}$. Additionally, to prevent the momentum from turning hyperbolic when $\beta = 0$ — that is, a purely polymeric fluid — a both-sides-diffusion technique introduced in [26] is applied, whereby $\nabla\cdot\left(\frac{(1-\beta)\mu}{Re}\nabla\boldsymbol{u}\right)$ is subtracted from both the implicit and explicit sides of the equation.

In treating the explicit convective terms, a high resolution total variation diminishing (TVD) scheme called CUBISTA [6] based on a normalized variable diagram (NVD) formulation is implemented for all equation systems, except for the volume fraction transport. CUBISTA is formally third order and deduces an expression for a normalized variable $\hat{\varphi}$ on a face, $\hat{\varphi}_f$, as a function of its values $\hat{\varphi}_P$ in a cell centroid.

Following the approximations of [35,36,58], we employ Picard iterations k to solve the Poisson-Boltzmann nonlinear system for the n-th time step:

$$\left[\mathscr{L} - 2\alpha\delta\cosh(\alpha\psi^{n,k})\right]\psi^{n,k+1} = 2\delta\sinh(\alpha\psi^{n,k}) - 2\alpha\delta\psi^{n,k}\cosh(\alpha\psi^{n,k}),$$

in which $\mathscr{L}$ denotes a numerical discretization of the laplacian $\nabla\cdot(\varepsilon_e\nabla)$, calculated by a 5-point stencil.

4.1 Computational VOF

The initialization of the volume fraction is done through an approximation of the initial interface surface by a regular value of an implicit function ϕ_σ. The configuration is determined through a Marching Squares-like algorithm, where cells are evaluated based on the signs of ϕ_σ at their vertices. Cells are assigned values of $f = 1$ or $f = 0$ when all vertices share the same sign, while mixed-sign cases require calculating the area of truncated polygons formed by edge intersections with the interface. Whenever there is ambiguity, cells are repeatedly refined into subcells until volume fraction values can be distinguished.

The method employs a normal vector calculation approach based on Shirani's method [47], utilizing a 7-point stencil for each direction, which was shown to give more accurate and cohesive results for relatively coarse meshes in [49]. The curvature is computed using a fixed stencil Height Function (HF) method, adapted from [44], which uses local explicit functions $h(y)$ to determine interface height and calculates curvature by $\frac{h''}{\left(1+(h')^2\right)^{3/2}}$, and employs either 3×7 or 7×3 stencils depending on which normal direction is greater. For degenerate cases, a weighted average is used to evaluate curvature at cell faces.

Interface reconstruction uses the PLIC (Piecewise Linear Interface Calculation) method, where interface segments satisfy the equation $\boldsymbol{n}_\sigma \cdot \boldsymbol{x} = \alpha_\sigma$ in cell-center coordinates. The value of α_σ is calculated through a quadratic equation involving the truncated polygon area, with careful consideration of cell geometry and normal vector orientation. The advection of the interface employs a split scheme following Puckett's approach [45], solving the conservative form of (2.2) with source terms, which alternates between implicit and explicit directional solving to achieve second order accuracy in time. The fluxes are calculated geometrically instead of using classical advection schemes to minimize numerical diffusion, guarantee volume conservation and mantain constraints on f, whereby the area going through cell faces on a given timestep is calculated based on a quadratic equation set by the interface configuration and velocity vector. For a detailed description of the algorithm check [48].

5 RESULTS

5.1 Boundary conditions and parameters

The boundary conditions are explicited in Figure 2, where we consider a rectangular channel of domain closure $[0,4]\times[-1,1]$. In the electroosmotic simulations, the adimensional wall values are $\zeta_T = -1 = -\zeta_B$ and $U_T = U_B = 0$, whereas neutral shear is done by imposing $U_T = 1 = -U_B$. We call this setup the asymmetric configuration [4,46], unlike a lot of parallel plate cases covered in the literature where both walls have the same potentials and velocities [39, 53, 57], which we refer to as the symmetric configuration. Regarding stress, due to hiperbolicity, the conformation tensor respects homogenous Neumann boundary conditions $\frac{\partial \boldsymbol{A}}{\partial \boldsymbol{n}} = \boldsymbol{0}$ in walls, inlet and outlet, and is initialized as the identity tensor.

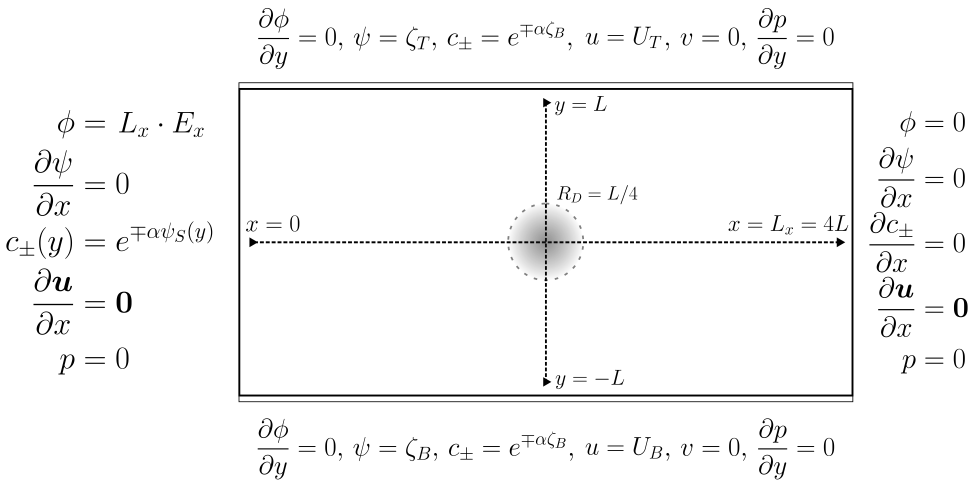

Figure 2: Adimensional boundary conditions of simulated flows.

Following a superposition of analytical solutions of the one-dimensional nonlinear Poisson-Boltzmann equation on walls [23, 32, 40], the initial horizontal velocity u in two-phase electroosmotic simulations is set to

$$u_0(x,y) = \frac{4}{\alpha}\left[\operatorname{arctanh}\left(\tanh\left(-\frac{\alpha}{4}\right)e^{\kappa(y-1)}\right) + \operatorname{arctanh}\left(\tanh\left(\frac{\alpha}{4}\right)\exp^{-\kappa(y+1)}\right)\right] + y, \quad (5.1)$$

$u_0(x,y) = y$ for neutral tests, the charge concentrations are initially set to 1, and the remaining properties are initialized as 0. A 5-level refinement mesh with square cells of length going from $1/32$ to $1/512$ is used for the singlephase simulations while the neutral and electroosmotic two-phase regimes are simulated in 512×256 and 768×384 uniform meshes, respectively. The numerical experiments are run in parallel on the Euler-CeMEAI high performance computer nodes.

The adimensional EOF and viscoelastic parameters are set to

$$Re = 0.01821,\ \alpha = 1,\ E_x = 38.94,\ \kappa = 32,\ Pe = 4.553,\ De = 0.4,\ \beta = 0.5,\ \varepsilon = 0.01,$$

with an additional near-linear singlephase case for comparison purposes where

$$Re = 1.821 \cdot 10^{-5},\ \alpha = 0.01,\ E_x = 3894,\ Pe = 0.04553,$$

since $\alpha = 0.01$ implies the exponential is almost linear. Moreover, the multiphase constants are chosen to be

$$Ca = 2.4,\ \rho_i = \mu_i = 1,$$

where $De_i = De$ and $\beta_i = \beta$ whenever fluid i is viscoelastic, the drop radius is $R_D = 0.25$, and Δt is set to $5 \cdot 10^{-5}$ in the PNP regime and $5 \cdot 10^{-4}$ for PB. For the variable permittivity simulations, $\varepsilon_{e_i} = 0.5, 0.1$ for either the drop or matrix, while the other fluid j has $\varepsilon_{e_j} = 1$. In the newtonian case, we also test polarities of $\varepsilon_{e_i} = 1/40 = 0.025$.

5.2 Asymmetric (Shear) Singlephase Electroosmotic Flow

With the time scales adjusted by the Reynolds number, Figure 4 shows the near-linear ($\alpha = 0.01$) transients develop slightly later. The velocity is increased by electroosmotic force near the walls and transferred to the center of the channel until it reaches an essentially shear profile at the channel center in a steady state (Figure 5) a phenomenon that occurs faster than in the symmetric case, seen in Figure 3. Moreover, it is observed through Figure 5 that the $\alpha = 0.01$ situation has a similar (but not identical) behavior to $\alpha = 1.0$ when the scales are adjusted. It should be noted that the Poisson-Nernst-Planck system has high instability, which we verified is increased by the asymmetric configuration in our simulations. For this reason and the fact that the time scales for velocity development were shown to be not significant for the electroosmotic situations in drop shearing, the two-phase comparisons are presented under Poisson-Boltzmann.

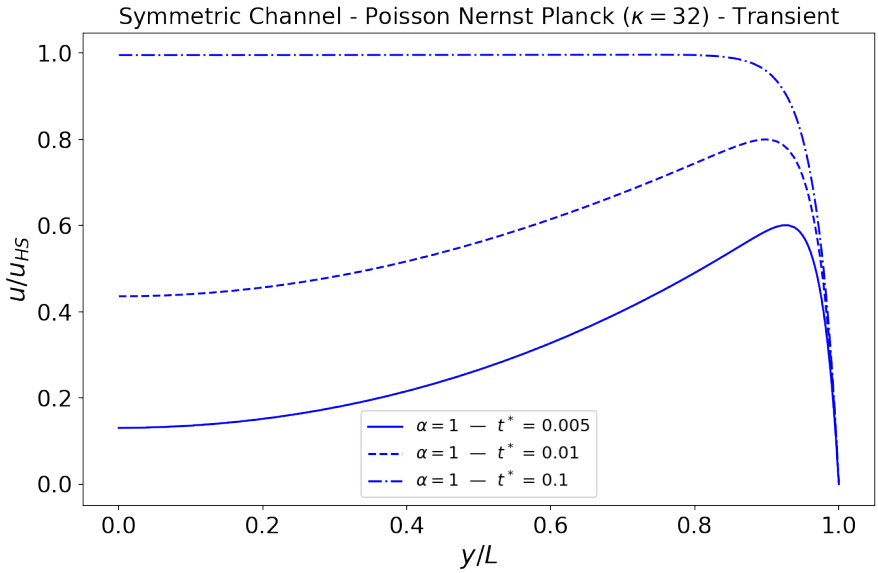

Figure 3: Transient u profiles during symmetric EOF — $\alpha = 1.0$ — under Poisson-Nernst-Planck. u_{HS} is the Helmholtz-Smoluchovski solution derived in detail by Kirby [32].

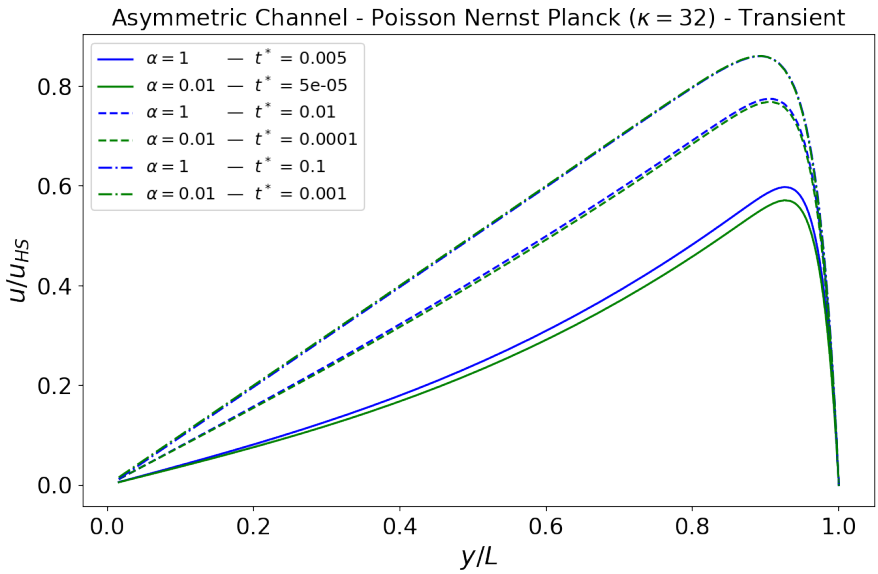

Figure 4: Transient u profiles during asymmetric EOF — $\alpha = 1.0$ vs $\alpha = 0.01$ (near-linear) — under Poisson-Nernst-Planck. u_{HS} is the Helmholtz-Smoluchovski solution derived in detail by Kirby [32].

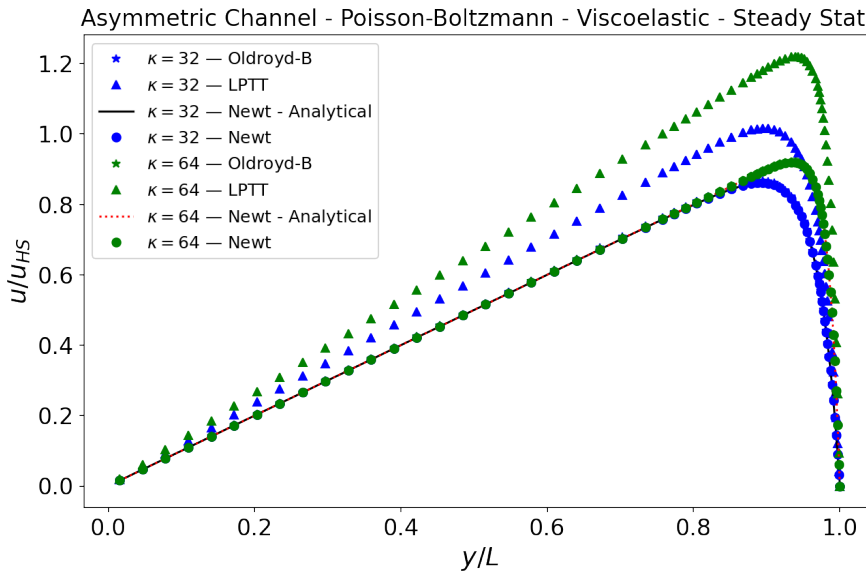

Figure 5: Steady-state u profiles in viscoelastic asymmetric EOF — analytical solutions as explicited in expression 5.1 and derived in detail by Kirby and others [32, 40], with a similar superposition for symmetric potentials as that of Garcia [23]. u_{HS} is the Helmholtz-Smoluchovski solution derived in detail by Kirby [32].

5.3 Drop Shearing — Neutral and Electroosmotic of uniform permittivity

This subsection reports the electroosmotic shearing flows, where the setting is validated by comparison with the neutral viscoelastic shearing of [20] and [16], which consider a pure Couette flow with walls moving in opposite directions, shearing a drop initially arranged in the rectangular domain center having radius $R_D = 0.25$, deformed with a constant shear rate $\dot{\gamma}$. Adapting their adimensional parameters to the ones defined in (2.2),

$$Re = 4.8, \quad Ca = 2.4, \quad De = 0.4, \quad \beta = 0.5, \quad \rho_0 = \rho_1 = \mu_0 = \mu_1 = 1$$

are obtained since u_{ref}, L are used instead of $R_D\dot{\gamma}$, R_D for the reference scales, with the adimensionalized times being the same. A property of interest is the commonly named deformation parameter, $\Phi_D = \frac{R_{\max} - R_{\min}}{R_{\max} + R_{\min}}$, defined according to the maximum and minimum radii, $R_{\max}(t)$ and $R_{\min}(t)$ of the drop at a given time t. Essentially a normalized measure of how strained the drop is. The matrix-drop configurations are abbreviated as NN, when both fluids are newtonian, NO, when the drop is an Oldroyb-B fluid and the matrix is newtonian, ON when vice versa and OO whenever both are Oldroyd-B. We should point out that the convention of NO and ON are opposite to [20] and [16].

Let P, Q be two finite sets of points of the plane. We define the Hausdorff distance between them as

$$\mathscr{H}(P,Q) := \max\left(\max_{p\in P}\min_{q\in Q}\|p-q\|_2, \max_{q\in Q}\min_{p\in P}\|p-q\|_2\right),$$

which encodes the largest of the distances from each point in one set to the whole of the other set. Results of the deformation parameter history and the PLIC geometry at time $t^* = 10$ were reproduced from Figueiredo [21] with a good accuracy; deformation parameters with their maximum differences not exceeding 2% are shown in Figure 6, and drop geometries with their corresponding Hausdorff distances are indicated in Figure 7, none of which are larger than $2 \cdot 10^{-3}$.

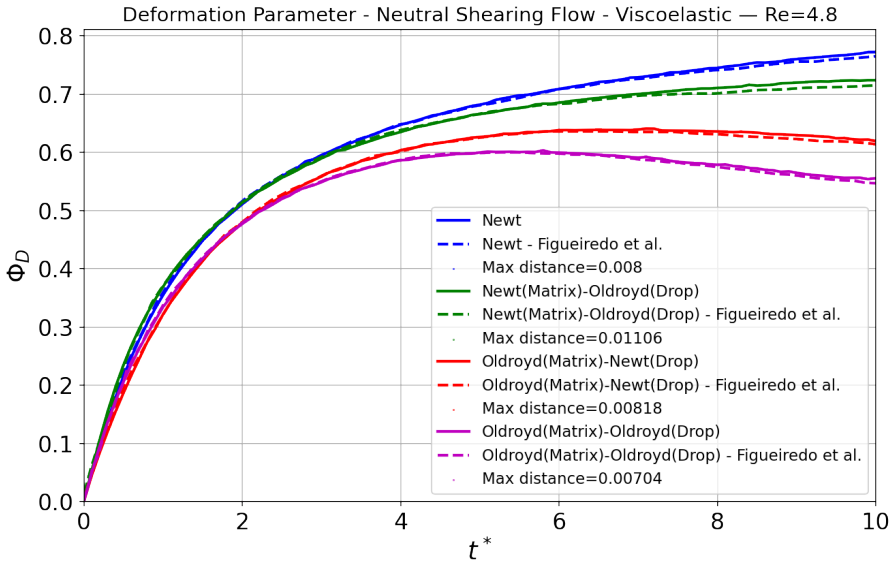

Figure 6: Comparison with [20] of the deformation parameters of neutral Couette shearing for various viscoelastic configurations of the matrix-drop system over time. Their maximum distances to each other are indicated for each comparison pair.

A neutral shear comparison between the Reynolds number used in electroosmotic flows, 0.01821, and the one from [21], 4.8, is shown in Figure 8 to illustrate the two-phase interface. Note that the order between the fluid types is maintained — flows with viscoelastic matrix lead to less drop deformation, with the OO case being the least deformed. In fact, image 8 suggests that the differences in the structure of the interface deformation tend to be relatively conserved between the different Reynolds flows, that is, the NN and ON drops, other than being more stretched are slightly pinched in their middle region, resembling dumbells, in contrast to OO and ON, which are more spherical with the presence of matrix viscoelasticity. These effects have lower magnitude for the smaller Reynolds situation, probably due to the greater surface response compared to shearing.

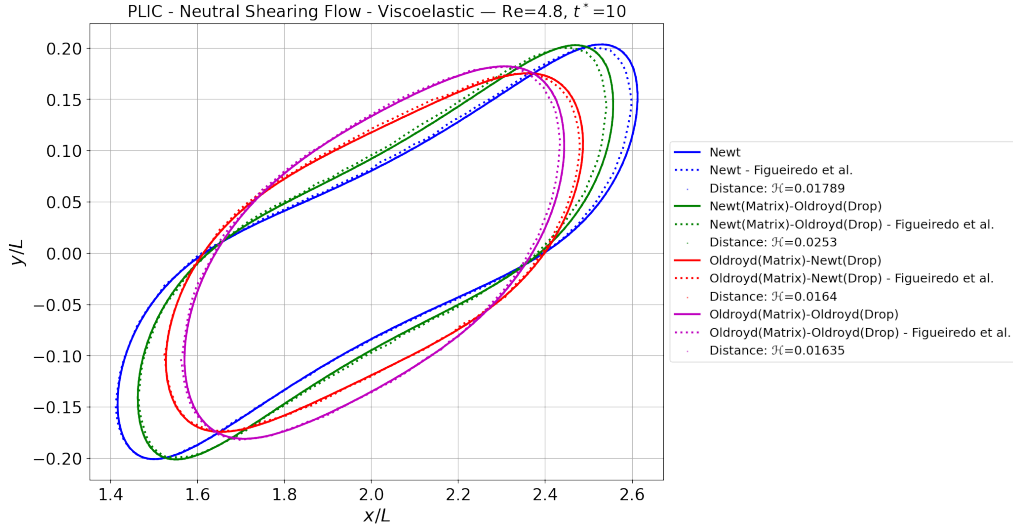

Figure 7: Comparison with [20] of two-phase interface of neutral Couette shearing for various viscoelastic configurations of the matrix-drop system — $t^* = 10.0$. Hausdorff distances are indicated for each comparison pair.

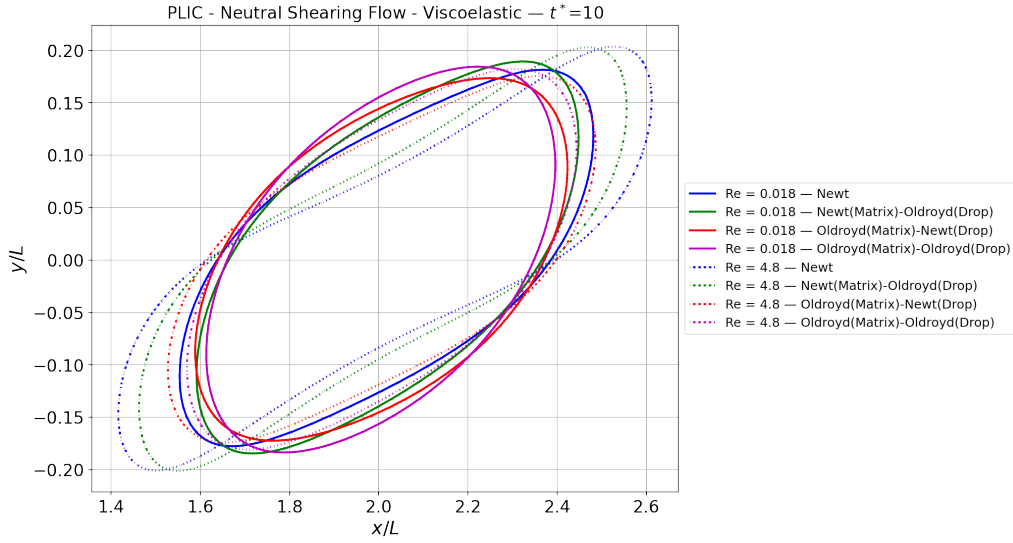

Figure 8: Two-phase interface of neutral Couette shearing for various viscoelastic configurations of the matrix-drop system — $Re = 4.8$ vs $Re = 0.01821$ — $t^* = 10.0$.

The deformation parameter comparison is exhibited in Figure 9. A strong similarity is verified, both in magnitude and shape of deformation, as well as PLIC geometry (see Figure 10), due to the close shear rate experienced by the drop in electroosmotic and neutral flows, as is evidenced by equation 5.2. Indeed, a differentiation of the expression 5.1 shows that the adimensional effective shear rate far enough from the walls is

$$\dot{\gamma}_{EO} = 1 - \frac{\frac{2}{\alpha}\log\left(\frac{\alpha+\sqrt{4\kappa^2+\alpha^2}}{2\kappa}\right)}{1-\frac{1}{\kappa}\log\left(\frac{a_T}{\alpha}\left(2\kappa+\sqrt{4\kappa^2+\alpha^2}\right)\right)}, \tag{5.2}$$

which gets very close to unit, like the neutral shear, as κ and α are increased.

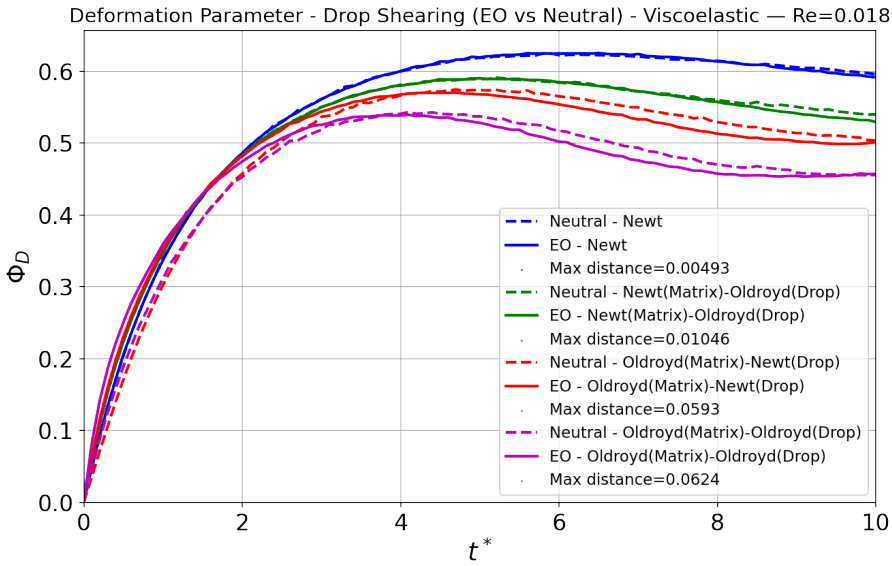

Figure 9: Deformation parameter of electroosmotic vs neutral shearing for different matrix-drop system viscoelastic configurations. The maximum distances to each other are indicated for each comparison pair.

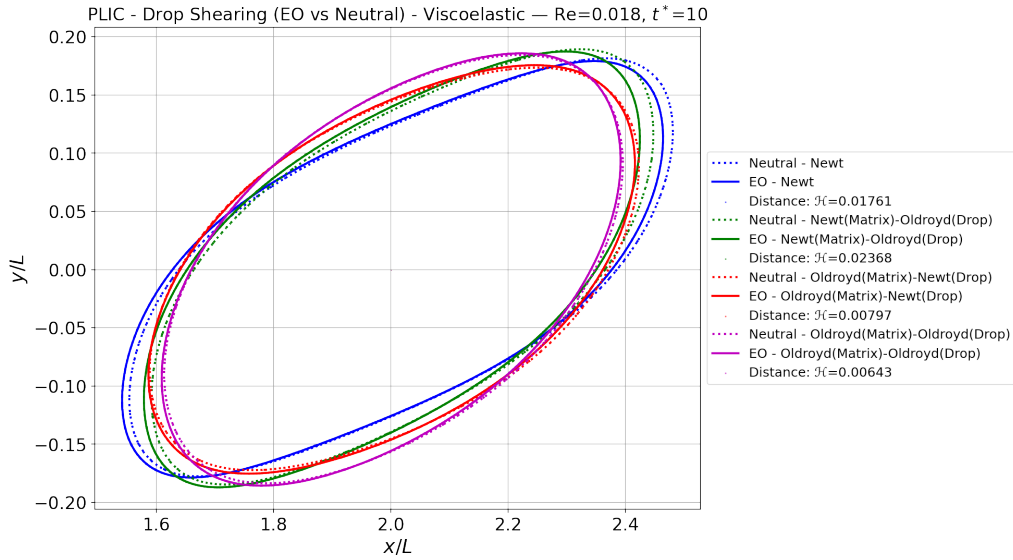

Figure 10: Two-phase interface of electroosmotic vs neutral shearing for different matrix-drop system viscoelastic configurations. Hausdorff distances are indicated for each comparison pair.

6 ELECTROOSMOTIC DROP SHEARING OF VARIABLE PERMITTIVITY

According to the Laplace equation of the applied potential, the permittivities alter the distribution of ϕ, which becomes transient and dependent on the interface arrangement. Its profiles at initial times in the channel cross-section are plotted in Figure 11. The different directions of the gradient of $\nabla\varepsilon_e$ in $\varepsilon_e\nabla^2\phi = -\nabla\varepsilon_e\cdot\nabla\phi$ are responsible for the clear symmetry observed relative to the uniform case. From the Poisson-Boltzmann system, less permittivity directly implies a smaller charge density, the influence of which, in the electric force, leads to smaller velocities and a steeper ψ distribution similar to a finer EDL when the matrix is less polarizable than the reference value. Less deformed drops in a more apolar matrix can be verified in Figures 12 and 13.

Considering ρ_e is not significant away from walls and the applied potential for varied polarities has a small difference near them, the only term in the mathematical modeling that can justify the large differences in drop shapes and orientations when the drop dielectric constant is varied is

$$-\frac{1}{2}\|\nabla(\phi+\psi)\|^2\nabla\varepsilon_e \approx -\frac{E_x^2}{2}\nabla\varepsilon_e,$$

included in the Korteweg-Helmholtz force and whose influence is similar to surface tension, but which acts uniformly on the interface and following the direction of $\nabla\varepsilon_e$. Such effect is responsible for the distinct interface geometries represented in Figure 14, which tend to rotate and deform more, particularly when $\varepsilon_{e_1} = 0.1$ and $\varepsilon_{e_1} = 0.025$, and get more spherical when $\varepsilon_{e_1} = 0.5$.

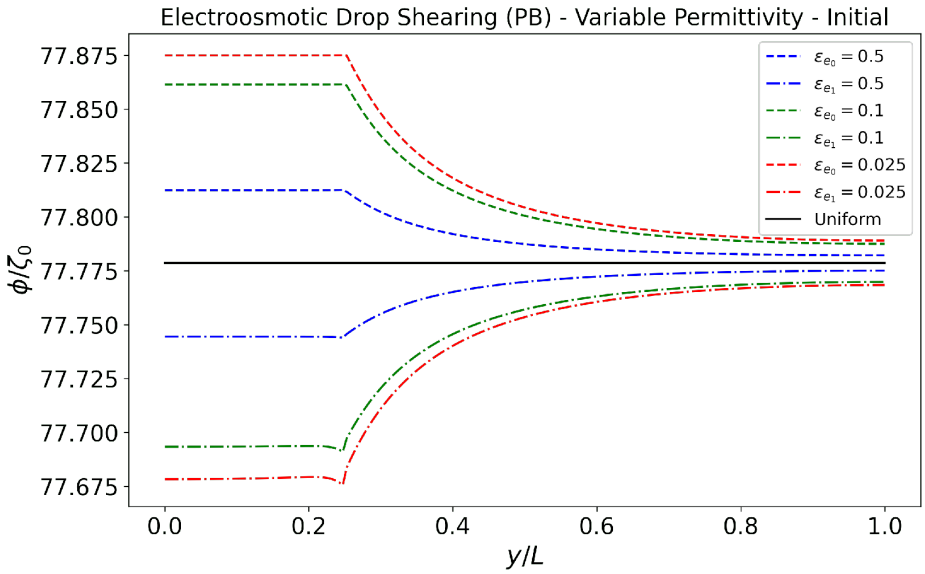

Figure 11: Applied potential in electroosmotic shearing for various permittivities of the matrix-drop system.

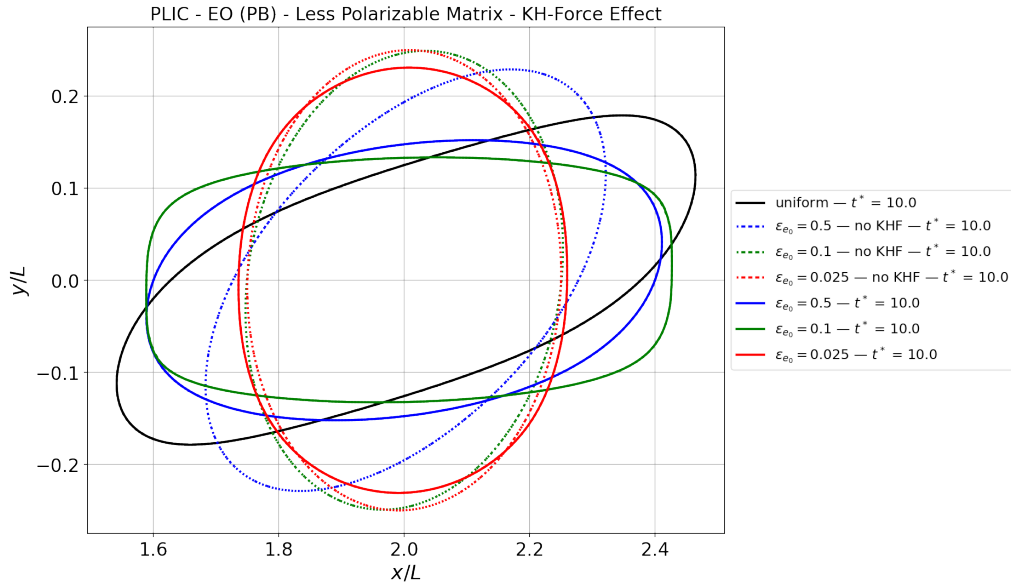

Figure 12: Two-phase interface of eletroosmotic shearing for different matrix permittivities with and without influence of the $\nabla\varepsilon_e$ term in the Korteweg-Helmholtz Force — $t^* = 10.0$.

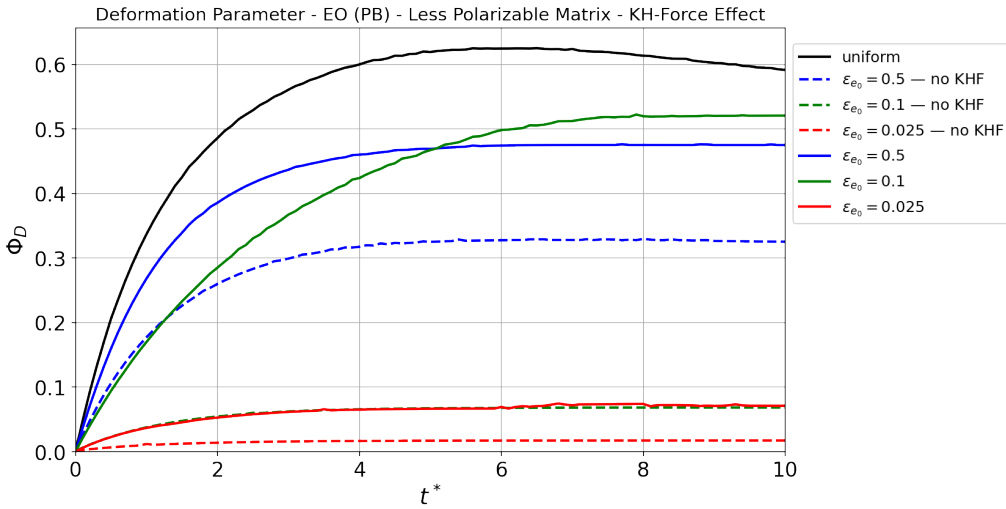

Figure 13: Deformation parameter of eletroosmotic shearing for different matrix permittivities with and without influence of the $\nabla\varepsilon_e$ term in the Korteweg-Helmholtz Force.

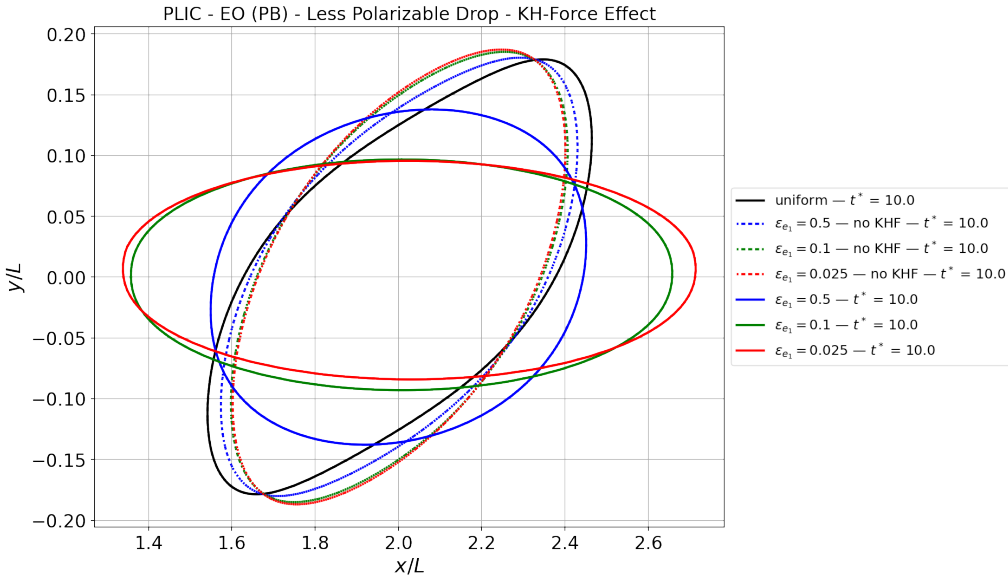

Figure 14: Two-phase interface of eletroosmotic shearing for different drop permittivities with and without influence of the $\nabla\varepsilon_e$ term in the Korteweg-Helmholtz Force — $t^* = 10.0$.

Similarly to the case of a less polar drop, the Korteweg-Helmholtz term has a complicated interaction with the droplet shapes when the matrix is of lower permittivity. Figure 12 also shows that when $\varepsilon_{e_0} = 0.025$, there is not much difference in the interface configuration, while it is induced

to orient itself in the flow direction for other permittivities. The situation of $^1/_{10}$ is the one that varies the most with the presence of such force, as well evidenced in illustration 13, possibly due to the combination of low shear and high variation of ε_e between the fluids. A comparison of the deformations of all permittivities of the matrix-drop system can be seen in Figure 15.

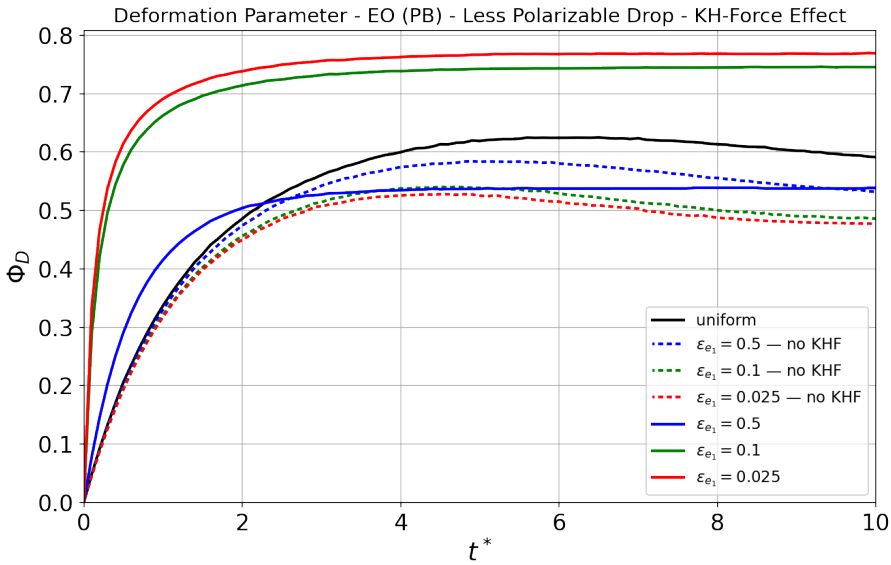

Figure 15: Deformation parameter of eletroosmotic shearing for different drop permittivities with and without influence of the $\nabla\varepsilon_e$ term in the Korteweg-Helmholtz Force.

The viscoelastic patterns are quite close to the newtonian ones. Indeed, comparing Figure 17, in which only the droplet is Oldroyd-B, with Figure 16, one notices the same order of deformation parameter profiles, although with the slight drop in deformation near $t^* = 7$ characteristic of this regime, especially in the uniform situation, seen in Figure 9. This drop occurs earlier when the matrix is Oldroyd-B (Figure 18), near $t^* = 5$, making the droplet in uniform permittivity less deformed than the apolar one with $\varepsilon_{e_1} = 0.5$. The restitution of the uniform case is even more pronounced when both fluids are viscoelastic, as shown in Figure 19, where we verify that the uniform condition ends with the *lowest* deformation among the polarities. Overall, we identify that the non-uniform cases stabilize the deformation more quickly and the KHF may be responsible for counterbalancing the shear forces and surface tension, since it acts in the same way across the entire interface, stabilization that we also observed in the stress profiles when both fluids are Oldroyd. According to the interfaces reconstructed by PLIC at $t^* = 10.0$, the force is also potentially responsible for keeping the droplets more spherical, unless they are sufficiently apolar.

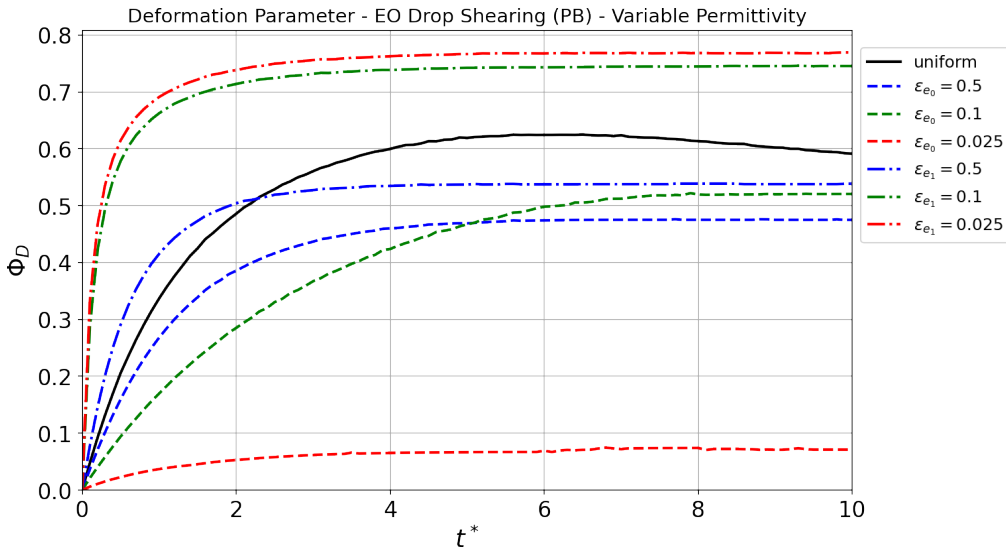

Figure 16: Deformation parameter of eletroosmotic shearing for various permittivities of the matrix-drop system.

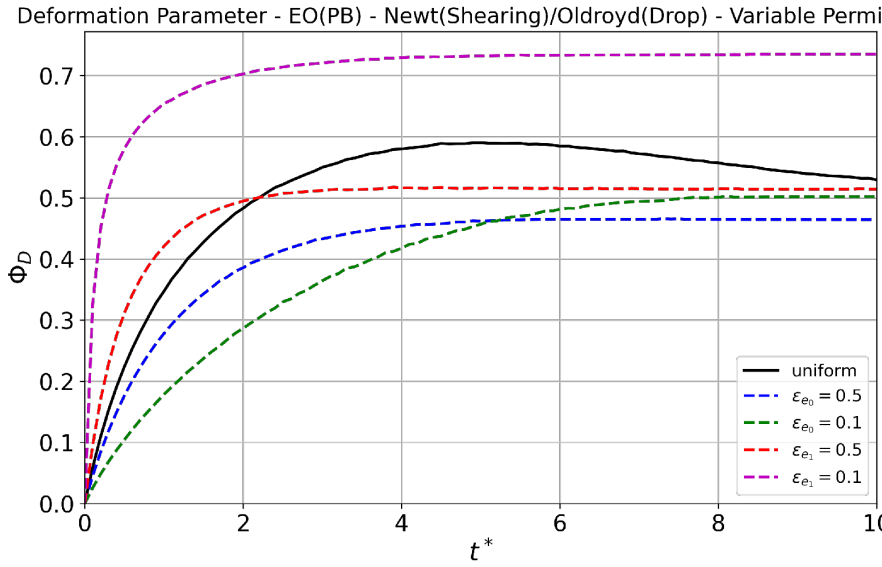

Figure 17: Deformation parameter of eletroosmotic shearing for different drop permittivities of the newtonian matrix and viscoelastic drop under Oldroyd-B.

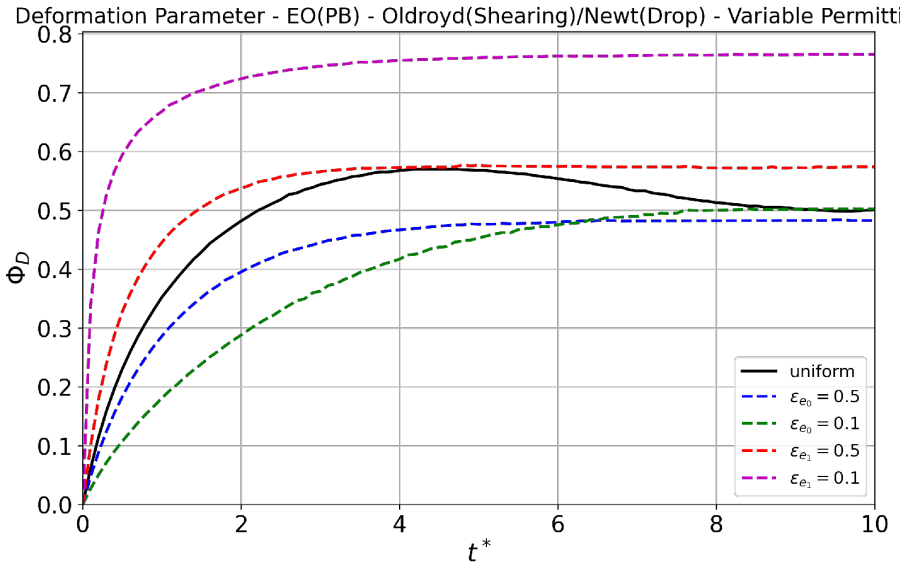

Figure 18: Deformation parameter of eletroosmotic shearing for different drop permittivities of the viscoelastic matrix and newtonian drop under Oldroyd-B.

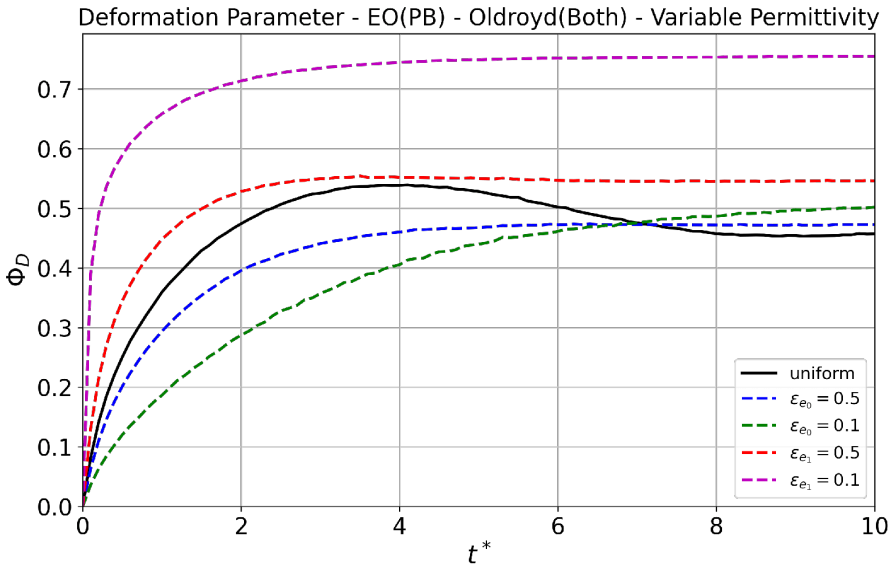

Figure 19: Deformation parameter of eletroosmotic shearing for different drop permittivities of the matrix and drop, both viscoelastic under Oldroyd-B.

7 CONCLUSION

This research reveals that electroosmotic shearing of uniform permittivity is very similar to neutral shearing in fine EDL regimes. Additionally, droplet deformation patterns at interfaces are significantly influenced by the Korteweg-Helmholtz permittivity gradient term, which generates a uniform surface force along the interface, with its direction determined by which fluid exhibits lower polarity. Viscoelasticity, when present in various matrix-droplet configurations helps reduce the velocity profile distortion caused by surface tension and leads to a more pronounced decrease in the deformation parameter over time. It also enables faster stabilization of deformations in cases of non-uniform permittivity, likely due to the balanced interaction between shearing forces, surface tension, and electrostatic effects at the interface. For future research, we suggest pressure difference studies, more complex geometries, comparative analysis of other complex fluid models, adaptive meshes, polyphasic flows, and three-dimensional simulations. We aim to contribute to understanding transient electrokinetic phenomena in complex systems and inform and inspire future multiphase electroosmosis simulations, particularly for microfluidic applications involving complex fluids, droplet formation, and Lab-on-a-Chip devices.

Data availability

Datasets related to this article are available upon request to the corresponding author.

Associate editor: Rosane Ushirobira

REFERENCES

[1] A. Afonso, M. Alves & F. Pinho. Analytical solution of mixed electro-osmotic/pressure driven flows of viscoelastic fluids in microchannels. *Journal of Non-Newtonian Fluid Mechanics*, **159**(1-3) (2009), 50–63. doi:10.1016/j.jnnfm.2009.01.006. URL `https://linkinghub.elsevier.com/retrieve/pii/S0377025709000184`.

[2] A. Afonso, M. Alves & F. Pinho. Analytical solution of two-fluid electro-osmotic flows of viscoelastic fluids. *Journal of Colloid and Interface Science*, **395** (2013), 277–286. doi:10.1016/j.jcis.2012.12.013. URL `https://linkinghub.elsevier.com/retrieve/pii/S0021979712013884`.

[3] A. Afonso, F. Pinho & M. Alves. The kernel-conformation constitutive laws. *Journal of Non-Newtonian Fluid Mechanics*, (2011), S0377025711002370. doi:10.1016/j.jnnfm.2011.09.008. URL `https://linkinghub.elsevier.com/retrieve/pii/S0377025711002370`.

[4] A.M. Afonso, M.A. Alves & F.T. Pinho. Electro-osmotic flow of viscoelastic fluids in microchannels under asymmetric zeta potentials. *Journal of Engineering Mathematics*, **71**(1) (2011), 15–30. doi:10.1007/s10665-010-9421-9. URL `http://link.springer.com/10.1007/s10665-010-9421-9`.

[5] A.M. Afonso, F.T. Pinho & M.A. Alves. Electro-osmotic flows of viscoelastic fluids: a numerical study. In "III Conferência Nacional em Mecânica de Fluidos, Termodinâmica e Energia (MEFTE - Bragança 09)" (2009).

[6] M.A. Alves, P.J. Oliveira & F.T. Pinho. A convergent and universally bounded interpolation scheme for the treatment of advection. *International Journal for Numerical Methods in Fluids*, **41**(1) (2003), 47–75. doi:10.1002/fld.428. URL https://onlinelibrary.wiley.com/doi/10.1002/fld.428.

[7] S. Balay, S. Abhyankar, M.F. Adams, J. Brown, P. Brune, K. Buschelman, L. Dalcin, V. Eijkhout, W.D. Gropp, D. Kaushik, M.G. Knepley, L.C. McInnes, K. Rupp, B.F. Smith, S. Zampini & H. Zhang. PETSc Web page (2015). URL http://www.mcs.anl.gov/petsc.

[8] G.K. Batchelor. "An Introduction to Fluid Dynamics". Cambridge University Press, 1st ed. (2000). doi:10.1017/CBO9780511800955.

[9] J. Bertoco, R.T. Leiva, L.L. Ferrás, A.M. Afonso & A. Castelo. Development Length of Fluids Modelled by the gPTT Constitutive Differential Equation. *Applied Sciences*, **11**(21) (2021), 10352. doi:10.3390/app112110352. URL https://www.mdpi.com/2076-3417/11/21/10352.

[10] W.D.S. Bezerra. "Estudo numerico de escoamento viscoelastico e eletroosmotico com potenciais dependente do tempo". Doutorado em Ciências de Computação e Matematica Computacional, Universidade de São Paulo, São Carlos (2019). doi:10.11606/T.55.2019.tde-25032019-143632. URL http://www.teses.usp.br/teses/disponiveis/55/55134/tde-25032019-143632/.

[11] W.S. Bezerra & A. Castelo. Simulação Numerica de Escoamento Eletroosmotico Usando o Modelo Constitutivo de Phan-Thien-Tanner. *TEMA (São Carlos)*, **21**(3) (2020), 461. doi:10.5540/tema.2020.021.03.461. URL https://tema.sbmac.org.br/tema/article/view/1271.

[12] J. Brackbill, D. Kothe & C. Zemach. A continuum method for modeling surface tension. *Journal of Computational Physics*, **100**(2) (1992), 335–354. doi:10.1016/0021-9991(92)90240-Y. URL https://linkinghub.elsevier.com/retrieve/pii/002199919290240Y.

[13] G. Chatzipirpiridis, A. Sanoria, O. Ergeneman, J. Sort, J. Puigmartí-Luis, B.J. Nelson, E. Pellicer & S. Pané. The electrochemical manipulation of apolar solvent drops in aqueous electrolytes by altering the surface polarity of polypyrrole architectures. *Electrochemistry Communications*, **54** (2015), 32–35. doi:10.1016/j.elecom.2015.02.014. URL https://linkinghub.elsevier.com/retrieve/pii/S1388248115000569.

[14] C.H. Chen. Electrohydrodynamic Stability. In A. Ramos (editor), "Electrokinetics and Electrohydrodynamics in Microsystems". Springer Vienna, Vienna (2011), p. 177–220. doi:10.1007/978-3-7091-0900-7_6. URL http://link.springer.com/10.1007/978-3-7091-0900-7_6.

[15] J. Chen, L.C. McInnes & H. Zhang. Analysis and Practical Use of Flexible BiCGStab. *Journal of Scientific Computing*, **68**(2) (2016), 803–825. doi:10.1007/s10915-015-0159-4. URL http://link.springer.com/10.1007/s10915-015-0159-4.

[16] T. Chinyoka, Y. Renardy, M. Renardy & D. Khismatullin. Two-dimensional study of drop deformation under simple shear for Oldroyd-B liquids. *Journal of Non-Newtonian Fluid Mechanics*, **130**(1) (2005), 45–56. doi:10.1016/j.jnnfm.2005.07.005. URL https://linkinghub.elsevier.com/retrieve/pii/S0377025705001710.

[17] S. Dhinakaran, A.M. Afonso, M.A. Alves & F.T. Pinho. Steady flow of viscoelastic fluids in microchannels under electrokinetic forces: PTT model with a Gordon–Schowalter convected derivative.

In “III Conferência Nacional em Mecânica de Fluidos, Termodinâmica e Energia (MEFTE - Bragança 09)” (2009).

[18] E.A.S. Doherty, R.J. Meagher, M.N. Albarghouthi & A.E. Barron. Microchannel wall coatings for protein separations by capillary and chip electrophoresis. *ELECTROPHORESIS*, **24**(1-2) (2003), 34–54. doi:10.1002/elps.200390029. URL https://analyticalsciencejournals.onlinelibrary.wiley.com/doi/10.1002/elps.200390029.

[19] R. Fattal & R. Kupferman. Constitutive laws for the matrix-logarithm of the conformation tensor. *Journal of Non-Newtonian Fluid Mechanics*, **123**(2-3) (2004), 281–285. doi:10.1016/j.jnnfm.2004.08.008. URL https://linkinghub.elsevier.com/retrieve/pii/S0377025704002630.

[20] R. Figueiredo, C. Oishi, A. Afonso, I. Tasso & J. Cuminato. A two-phase solver for complex fluids: Studies of the Weissenberg effect. *International Journal of Multiphase Flow*, **84** (2016), 98–115. doi:10.1016/j.ijmultiphaseflow.2016.04.014. URL https://linkinghub.elsevier.com/retrieve/pii/S0301932215301294.

[21] R.A. Figueiredo. “Simulação numerica de escoamentos viscoelasticos multifasicos complexos”. Doutorado em Ciências de Computação e Matematica Computacional, Universidade de São Paulo, São Carlos (2016). doi:10.11606/T.55.2016.tde-30112016-160821. URL http://www.teses.usp.br/teses/disponiveis/55/55134/tde-30112016-160821/.

[22] M. Gao & L. Gui. A handy liquid metal based electroosmotic flow pump. *Lab Chip*, **14**(11) (2014), 1866–1872. doi:10.1039/C4LC00111G. URL https://xlink.rsc.org/?DOI=C4LC00111G.

[23] A.L. Garcia, L.K. Ista, D.N. Petsev, M.J. O’Brien, P. Bisong, A.A. Mammoli, S.R.J. Brueck & G.P. Lopez. Electrokinetic molecular separation in nanoscale fluidic channels. *Lab on a Chip*, **5**(11) (2005), 1271. doi:10.1039/b503914b. URL https://xlink.rsc.org/?DOI=b503914b.

[24] R.J. Gordon & W.R. Schowalter. Anisotropic Fluid Theory: A Different Approach to the Dumbbell Theory of Dilute Polymer Solutions. *Transactions of the Society of Rheology*, **16**(1) (1972), 79–97. doi:10.1122/1.549256. URL https://pubs.aip.org/jor/article/16/1/79/993857/Anisotropic-Fluid-Theory-A-Different-Approach-to.

[25] S. Guido & F. Greco. Dynamics of a Liquid Drop in a Flowing Immiscible Liquid. In “Rheology Reviews 2004”. British Society of Rheology (2004), p. 99–142.

[26] R. Guénette & M. Fortin. A new mixed finite element method for computing viscoelastic flows. *Journal of Non-Newtonian Fluid Mechanics*, **60**(1) (1995), 27–52. doi:10.1016/0377-0257(95)01372-3. URL https://linkinghub.elsevier.com/retrieve/pii/0377025795013723.

[27] F.H. Harlow & J.E. Welch. Numerical Calculation of Time-Dependent Viscous Incompressible Flow of Fluid with Free Surface. *The Physics of Fluids*, **8**(12) (1965), 2182–2189. doi:10.1063/1.1761178. URL https://pubs.aip.org/pfl/article/8/12/2182/951500/Numerical-Calculation-of-Time-Dependent-Viscous.

[28] V.E. Henson & U.M. Yang. BoomerAMG: A parallel algebraic multigrid solver and preconditioner. *Applied Numerical Mathematics*, **41**(1) (2002), 155–177. doi:10.1016/S0168-9274(01)00115-5. URL https://linkinghub.elsevier.com/retrieve/pii/S0168927401001155.

[29] C. Hirt & B. Nichols. Volume of fluid (VOF) method for the dynamics of free boundaries. *Journal of Computational Physics*, **39**(1) (1981), 201–225. doi:10.1016/0021-9991(81)90145-5. URL https://linkinghub.elsevier.com/retrieve/pii/0021999181901455.

[30] M.A. Hulsen. A sufficient condition for a positive definite configuration tensor in differential models. *Journal of Non-Newtonian Fluid Mechanics*, **38**(1) (1990), 93–100. doi:10.1016/0377-0257(90)85034-V. URL https://linkinghub.elsevier.com/retrieve/pii/037702579085034V.

[31] K. Kim, H.S. Kwak & T.H. Song. A numerical model for simulating electroosmotic micro- and nanochannel flows under non-Boltzmann equilibrium. *Fluid Dynamics Research*, **43**(4) (2011), 041401. doi:10.1088/0169-5983/43/4/041401. URL https://iopscience.iop.org/article/10.1088/0169-5983/43/4/041401.

[32] B.J. Kirby. "Micro- and Nanoscale Fluid Mechanics: Transport in Microfluidic Devices". Cambridge University Press, New York, NY (2010).

[33] C. Ko, D. Li, A. Malekanfard, Y. Wang, L. Fu & X. Xuan. Electroosmotic flow of non-Newtonian fluids in a constriction microchannel. *Electrophoresis*, **40**(10) (2019), 1387–1394. doi:10.1002/elps.201800315. URL https://analyticalsciencejournals.onlinelibrary.wiley.com/doi/10.1002/elps.201800315.

[34] R.G. Larson. "Constitutive equations for polymer melts and solutions". Butterworths series in chemical engineering. Butterworths, Boston (1988).

[35] M. Mirzadeh, M. Theillard & F. Gibou. A second-order discretization of the nonlinear Poisson–Boltzmann equation over irregular geometries using non-graded adaptive Cartesian grids. *Journal of Computational Physics*, **230**(5) (2011), 2125–2140. doi:10.1016/j.jcp.2010.12.008. URL https://linkinghub.elsevier.com/retrieve/pii/S0021999110006728.

[36] G. Mohiuddin Mala, C. Yang & D. Li. Electrical double layer potential distribution in a rectangular microchannel. *Colloids and Surfaces A: Physicochemical and Engineering Aspects*, **135**(1-3) (1998), 109–116. doi:10.1016/S0927-7757(97)00215-X. URL https://linkinghub.elsevier.com/retrieve/pii/S092777579700215X.

[37] M. Monteferrante, L. Sola, M. Cretich, M. Chiari, U. Marini Bettolo Marconi & S. Melchionna. Controlling electroosmotic flows by polymer coatings: A joint experimental-theoretical investigation. *The Journal of Chemical Physics*, **143**(18) (2015), 184907. doi:10.1063/1.4934998. URL https://pubs.aip.org/jcp/article/143/18/184907/562780/Controlling-electroosmotic-flows-by-polymer.

[38] J.G. Oldroyd. On the Formulation of Rheological Equations of State. *Proceedings of the Royal Society of London. Series A, Mathematical and Physical Sciences*, **200**(1063) (1950), 523–541. URL http://www.jstor.org/stable/98422.

[39] H. Park, J. Lee & T. Kim. Comparison of the Nernst–Planck model and the Poisson–Boltzmann model for electroosmotic flows in microchannels. *Journal of Colloid and Interface Science*, **315**(2) (2007), 731–739. doi:10.1016/j.jcis.2007.07.007. URL https://linkinghub.elsevier.com/retrieve/pii/S0021979707009629.

[40] H. Park & W. Lee. Helmholtz–Smoluchowski velocity for viscoelastic electroosmotic flows. *Journal of Colloid and Interface Science*, **317**(2) (2008), 631–636. doi:10.1016/j.jcis.2007.09.027. URL https://linkinghub.elsevier.com/retrieve/pii/S0021979707013380.

[41] H.M. Park & W.M. Lee. Effect of viscoelasticity on the flow pattern and the volumetric flow rate in electroosmotic flows through a microchannel. *Lab on a Chip*, **8**(7) (2008), 1163. doi:10.1039/b800185e. URL https://xlink.rsc.org/?DOI=b800185e.

[42] N.A. Patankar & H.H. Hu. Numerical Simulation of Electroosmotic Flow. *Analytical Chemistry*, **70**(9) (1998), 1870–1881. doi:10.1021/ac970846u. URL https://pubs.acs.org/doi/10.1021/ac970846u.

[43] S.V. Patankar. "Numerical Heat Transfer and Fluid Flow". CRC Press, Boca Raton, FL (2018).

[44] S. Popinet. An accurate adaptive solver for surface-tension-driven interfacial flows. *Journal of Computational Physics*, **228**(16) (2009), 5838–5866. doi:10.1016/j.jcp.2009.04.042. URL https://linkinghub.elsevier.com/retrieve/pii/S002199910900240X.

[45] E.G. Puckett, A.S. Almgren, J.B. Bell, D.L. Marcus & W.J. Rider. A High-Order Projection Method for Tracking Fluid Interfaces in Variable Density Incompressible Flows. *Journal of Computational Physics*, **130**(2) (1997), 269–282. doi:10.1006/jcph.1996.5590. URL https://linkinghub.elsevier.com/retrieve/pii/S0021999196955904.

[46] A.M. Ribau, L.L. Ferrás, M.L. Morgado, M. Rebelo, F.T. Pinho & A.M. Afonso. The effect of asymmetric zeta potentials on the electro-osmotic flow of a generalized Phan–Thien–Tanner fluid. *Journal of Engineering Mathematics*, **148**(1) (2024), 1. doi:10.1007/s10665-024-10387-7. URL https://link.springer.com/10.1007/s10665-024-10387-7.

[47] E. Shirani, N. Ashgriz & J. Mostaghimi. Interface pressure calculation based on conservation of momentum for front capturing methods. *Journal of Computational Physics*, **203**(1) (2005), 154–175. doi:10.1016/j.jcp.2004.08.017. URL https://linkinghub.elsevier.com/retrieve/pii/S0021999104003225.

[48] A.T.G.D. Silva. "Desenvolvimento da tecnica PLIC-VOF no sistema HiG-Flow para simulação de escoamentos bifasicos". Mestrado em Ciências de Computação e Matematica Computacional, Universidade de São Paulo, São Carlos (2020). doi:10.11606/D.55.2020.tde-22072020-142449. URL https://www.teses.usp.br/teses/disponiveis/55/55134/tde-22072020-142449/.

[49] A.T.G.d. Silva. Simulação numérica de escoamentos viscoelásticos bifásicos 2D e 3D utilizando o sistema HiGFlow (2022). PhD Progress Report.

[50] F. Sousa, C. Lages, J. Ansoni, A. Castelo & A. Simao. A finite difference method with meshless interpolation for incompressible flows in non-graded tree-based grids. *Journal of Computational Physics*, **396** (2019), 848–866. doi:10.1016/j.jcp.2019.07.011. URL https://linkinghub.elsevier.com/retrieve/pii/S0021999119304966.

[51] F.S. Sousa, C.M. Oishi & G.C. Buscaglia. Spurious transients of projection methods in microflow simulations. *Computer Methods in Applied Mechanics and Engineering*, **285** (2015), 659–693. doi:10.1016/j.cma.2014.11.039. URL https://linkinghub.elsevier.com/retrieve/pii/S0045782514004721.

[52] T.M. Squires & S.R. Quake. Microfluidics: Fluid physics at the nanoliter scale. *Reviews of Modern Physics*, **77**(3) (2005), 977–1026. doi:10.1103/RevModPhys.77.977. URL https://link.aps.org/doi/10.1103/RevModPhys.77.977.

[53] G. Tang, X. Li, Y. He & W. Tao. Electroosmotic flow of non-Newtonian fluid in microchannels. *Journal of Non-Newtonian Fluid Mechanics*, **157**(1-2) (2009), 133–137. doi:10.1016/j.jnnfm.2008.11.002. URL https://linkinghub.elsevier.com/retrieve/pii/S0377025708001948.

[54] M. Tarn & N. Pamme. Microfluidics. In "Reference Module in Chemistry, Molecular Sciences and Chemical Engineering". Elsevier (2014), p. B9780124095472053518. doi:10.1016/B978-0-12-409547-2.05351-8. URL https://linkinghub.elsevier.com/retrieve/pii/B9780124095472053518.

[55] N.P. Thien & R.I. Tanner. A new constitutive equation derived from network theory. *Journal of Non-Newtonian Fluid Mechanics*, **2**(4) (1977), 353–365. doi:10.1016/0377-0257(77)80021-9. URL https://linkinghub.elsevier.com/retrieve/pii/0377025777800219.

[56] M. Yamamoto. The Visco-elastic Properties of Network Structure I. General Formalism. *Journal of the Physical Society of Japan*, **11**(4) (1956), 413–421. doi:10.1143/JPSJ.11.413. URL https://journals.jps.jp/doi/10.1143/JPSJ.11.413.

[57] R.J. Yang, L.M. Fu & C.C. Hwang. Electroosmotic Entry Flow in a Microchannel. *Journal of Colloid and Interface Science*, **244**(1) (2001), 173–179. doi:10.1006/jcis.2001.7847. URL https://linkinghub.elsevier.com/retrieve/pii/S0021979701978476.

[58] R.J. Yang, L.M. Fu & Y.C. Lin. Electroosmotic Flow in Microchannels. *Journal of Colloid and Interface Science*, **239**(1) (2001), 98–105. doi:10.1006/jcis.2001.7551. URL https://linkinghub.elsevier.com/retrieve/pii/S0021979701975514.

How to cite

D.G.L. Raymundo, A.M.P. Afonso & A. Castelo Filho. Numerical simulations of two-phase electroosmotic shearing with viscoelastic fluids. *Trends in Computational and Applied Mathematics*, **26**(2025), e01843. doi: 10.5540/tcam.2025.026.e01843.